RESEARCH ARTICLE SUMMARY

GAS GIANT PLANETS

Close-range remote sensing of Saturn's rings during Cassini's ring-grazing orbits and Grand Finale

Matthew S. Tiscareno*, Philip D. Nicholson, Jeffrey N. Cuzzi, Linda J. Spilker, Carl D. Murray, Matthew M. Hedman, Joshua E. Colwell, Joseph A. Burns, Shawn M. Brooks, Roger N. Clark, Nicholas J. Cooper, Estelle Deau, Cecile Ferrari, Gianrico Filacchione, Richard G. Jerousek, Stéphane Le Mouélic, Ryuji Morishima, Stu Pilorz, Sébastien Rodriguez, Mark R. Showalter, Sarah V. Badman, Emily J. Baker, Bonnie J. Buratti, Kevin H. Baines, Christophe Sotin

INTRODUCTION: Saturn's rings are an accessible exemplar of astrophysical disk processes and a delicate tracer of the Saturn system's dynamical processes and history.

RATIONALE: During its ring grazing orbits and Grand Finale, the Cassini spacecraft passed very close to Saturn's main rings and obtained very high–spatial-resolution images, spectral scans, and temperature scans.

RESULTS: We find structures related to the detailed sculpting of rings by embedded masses, including structures near the moon Daphnis that have apparently experienced markedly different perturbations compared to the surrounding ring material, and complex structure elements within the largest propeller-shaped disturbances. Interpreting certain such elements in terms of the Hill radius yields diameters of 1.0 to 1.6 km for the largest propeller-causing moons.

Several classes of subkilometer structure in the ring, which we call textures, are found in well-defined radial bands, which in many cases are difficult to correlate with other ring properties. The plateaux in the C ring exhibit a characteristic streaky texture. We hypothesize that these textures indicate variation in properties that affect the results of particle-particle collisions.

Medium-strength density waves neither alter the spectral characteristics of the region sur-rounding them nor exclude swarms of propellers from their vicinity, as the largest-density waves are known to do. We also confirm that even the strongest bending waves (such as Mimas 5:3) do not exhibit any signs of spectral halos. However, medium-strength density waves do exhibit clumpy texture in their troughs, and they also alter the propeller size distribution.

"Mini-jets" in the F ring are found in clusters, whose members evolve in lockstep with each other. This provides the strongest evidence yet that impacts onto the rings are commonly due to (Saturn-orbiting) streams of material, rather than lone impacting objects.

The distinct light-scattering characteristics of the narrow region outward of the Keeler gap—weaker water ice absorption bands, higher reflectivity, grayish rather than reddish color—transition abruptly from the rest of the A ring, although different degrees of abruptness are seen in the visible and the near-infrared. The combination of weaker water-ice band depths with higher reflectivity is difficult to understand.

Water-ice band depth and general color slope are closely correlated with optical depth, and temperature is anticorrelated (that is, denser regions are colder), even in sharply banded regions, down to the spatial resolution limit of ~3 km px^{-1}. However, the narrow bright bands in the C ring, called plateaux, have similar color slopes and water-ice band depths to those of the surrounding C ring, despite their marked difference in brightness. Furthermore, denser regions are warmer in some fine-scaled structures, including C-ring plateaux and structure in the B ring, both on the lit side only, and strong waves in the A ring on both the lit and unlit sides.

CONCLUSION: The rings are sculpted by embedded masses, producing structure visible down to our resolution limit. Correlations of spectral properties and temperature with optical depth are tight at many locations, although exceptions are found that deepen puzzles in certain regions. Many of these results are likely related to radial stratification in particle properties, rather than in chemical composition or surface mass density. ∎
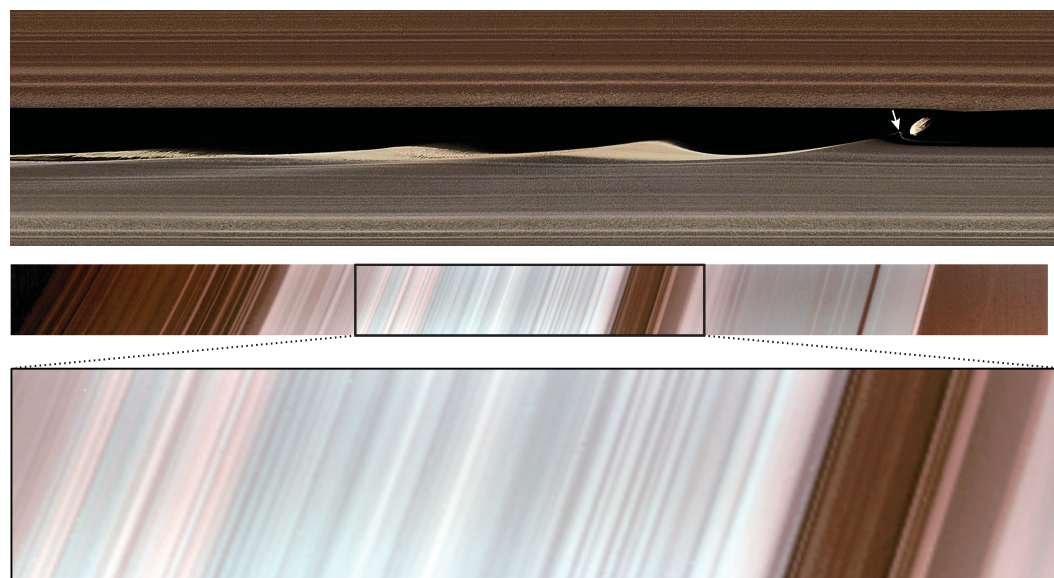
False-color images of Saturn's rings. (Top) A mosaic showing Daphnis in the Keeler gap on the lit side of the rings, with three wave crests of the structure raised by Daphnis in the gap's outer edge. (Middle and bottom) Visual and Infrared Mapping Spectrometer radial scans across the lit side of the main rings, displayed as false-color images. Reddish colors signify a higher fraction of components other than water ice. The boxed region in the middle panel indicates the location of the bottom panel.

RESEARCH ARTICLE

GAS GIANT PLANETS

Close-range remote sensing of Saturn's rings during Cassini's ring-grazing orbits and Grand Finale

Matthew S. Tiscareno[1]*, Philip D. Nicholson[2], Jeffrey N. Cuzzi[3], Linda J. Spilker[4], Carl D. Murray[5], Matthew M. Hedman[6], Joshua E. Colwell[7], Joseph A. Burns[2,8], Shawn M. Brooks[4], Roger N. Clark[9], Nicholas J. Cooper[5], Estelle Deau[4,10], Cecile Ferrari[11], Gianrico Filacchione[12], Richard G. Jerousek[7], Stéphane Le Mouélic[13], Ryuji Morishima[4,10], Stu Pilorz[1], Sébastien Rodriguez[11], Mark R. Showalter[1], Sarah V. Badman[14], Emily J. Baker[15], Bonnie J. Buratti[4], Kevin H. Baines[4], Christophe Sotin[4]

Saturn's rings are an accessible exemplar of an astrophysical disk, tracing the Saturn system's dynamical processes and history. We present close-range remote-sensing observations of the main rings from the Cassini spacecraft. We find detailed sculpting of the rings by embedded masses, and banded texture belts throughout the rings. Saturn-orbiting streams of material impact the F ring. There are fine-scaled correlations among optical depth, spectral properties, and temperature in the B ring, but anticorrelations within strong density waves in the A ring. There is no spectral distinction between plateaux and the rest of the C ring, whereas the region outward of the Keeler gap is spectrally distinct from nearby regions. These results likely indicate that radial stratification of particle physical properties, rather than compositional differences, is responsible for producing these ring structures.

S aturn's main rings (*1*) are the regions known as the A, B, C, and F rings and the Cassini Division, which together constitute a broad, dense disk of orbiting particles lying in the equatorial plane between 74,600 and 140,200 km (that is, 1.2 to 2.3 Saturn radii) from Saturn's center. The normal optical depth τ_n (*2*) in the main rings is at least $\tau_n \gtrsim 0.1$, and in some locations $\tau_n \gg 1$. Particle composition is dominated by water ice, with trace contaminants, and particle size ranges from millimeters to meters (although a few localities, including the F ring, are rich in dust). By contrast, the dusty rings are inward (the D ring) and outward (the E and G rings) of the main rings, have $\tau_n \ll 0.1$, and are dominated by micrometer-sized particles (*3*).

The 13-year mission of the Cassini spacecraft at Saturn culminated in two stages. During the ring-grazing orbits (RGOs), from December 2016 to April 2017, Cassini executed near-polar orbits that crossed the ring plane just outward of the F ring, providing close-range viewing of the outer portion of the main rings. During the Grand Finale (GF), from April to September 2017, the orbit shifted so that closest approach to Saturn was inward of the D ring, passing a few thousand km above Saturn's cloud tops, providing close-range flybys of the inner portion of the main rings. We present and analyze optical remote-sensing data taken during these flybys (*4*). We use data from Cassini's Imaging Science Subsystem (ISS) (*5*), Visual and Infrared Mapping Spectrometer (VIMS) (*6*), Composite Infrared Spectrometer (CIRS) (*7*), and Ultraviolet Imaging Spectrograph (UVIS) (*8*).

Ring structure: Embedded moons and propellers

Each ring particle follows its own orbit around the planet. However, collective effects, including collisions and mutual self-gravity, affect the structure of the rings, as do interactions with larger orbiting objects. Moons ranging in size from Titan to Pan raise spiral density and bending waves in the ring (*9–11*). Moderate-sized moons Pan (radius $R \sim 14$ km) and Daphnis ($R \sim 4$ km) orbit within the outer part of the A ring and clear sharp-edged gaps (the Encke and Keeler gaps, respectively). Smaller moons, but ones that are still substantially larger than the largest continuum ring particles, create local disturbances that have been dubbed "propellers," because of their shape (*12*).

Propellers are similar in principle to a circumferential gap like the Encke or Keeler gap, except that the embedded moon's influence is overcome some distance downstream as the gap is filled in by the viscosity of the disk. Swarms of relatively small propellers, likely due to embedded moons ~100 m in size, are present in the Propeller Belts of the mid-A ring (*13–15*). There are probably more than 10^6 propellers over the several-thousand-km annulus of the Propeller Belts (*15*). Solitary larger propellers, likely due to embedded moons ~1 km in size, orbit beyond the Encke gap (*16*). At least a half-dozen of the latter have had their orbits tracked for the duration of the Cassini mission, and their shifting orbital attributes have been analyzed theoretically (*12*).

Among the science objectives of the RGO and GF (presented in Fig. 1) were close-range flybys of Pan and Daphnis (*17*) and of three large propellers (namely, those nicknamed Blériot, Earhart, and Santos-Dumont), as well as high-resolution imaging of the Propeller Belts.

Daphnis and its vicinity

A false-color mosaic of Daphnis and its vicinity is shown in Fig. 1A. Daphnis itself is discussed in a companion paper (*17*); here we focus on the ring material perturbed by Daphnis. The image conveys the dichotomy in brightness and color that occurs at the Keeler gap (see below). Immediately to the lower left of Daphnis in Fig. 1A, within the gap, a strand of material is seen to follow a looping streamline. This material was likely pulled out of the sharp edge of the gap by a recent passage of Daphnis and is now spreading along its streamline as a result of Keplerian shear (*18*). Cassini was 13.5° above the ring plane when this image was taken, and the wavy edges of the Keeler gap are known to have a vertical component due to the orbital inclination of Daphnis (*19*), so the streamline seen here may be vertical and/or in-plane, which cannot be disentangled, owing to projection effects.

Downstream of Daphnis (which is trailing on the outer edge of the gap, but leading on the inner edge, due to Keplerian shear), the edge is scalloped with a characteristic wavelength equal to $3\pi\Delta a$, where Δa is the difference in semimajor axis between Daphnis and the gap edge (*12*). It was previously known that the wavy edges due to Daphnis die away only a few wave crests downstream, whereas those due to Pan in the edges of the Encke gap persist for the entire circumferential extent of the gap (*20–22*). Figure 1A shows structure in the third wave crest downstream of Daphnis. The trailing structure in the outer edge is seen on the left-hand side of Fig. 1A and
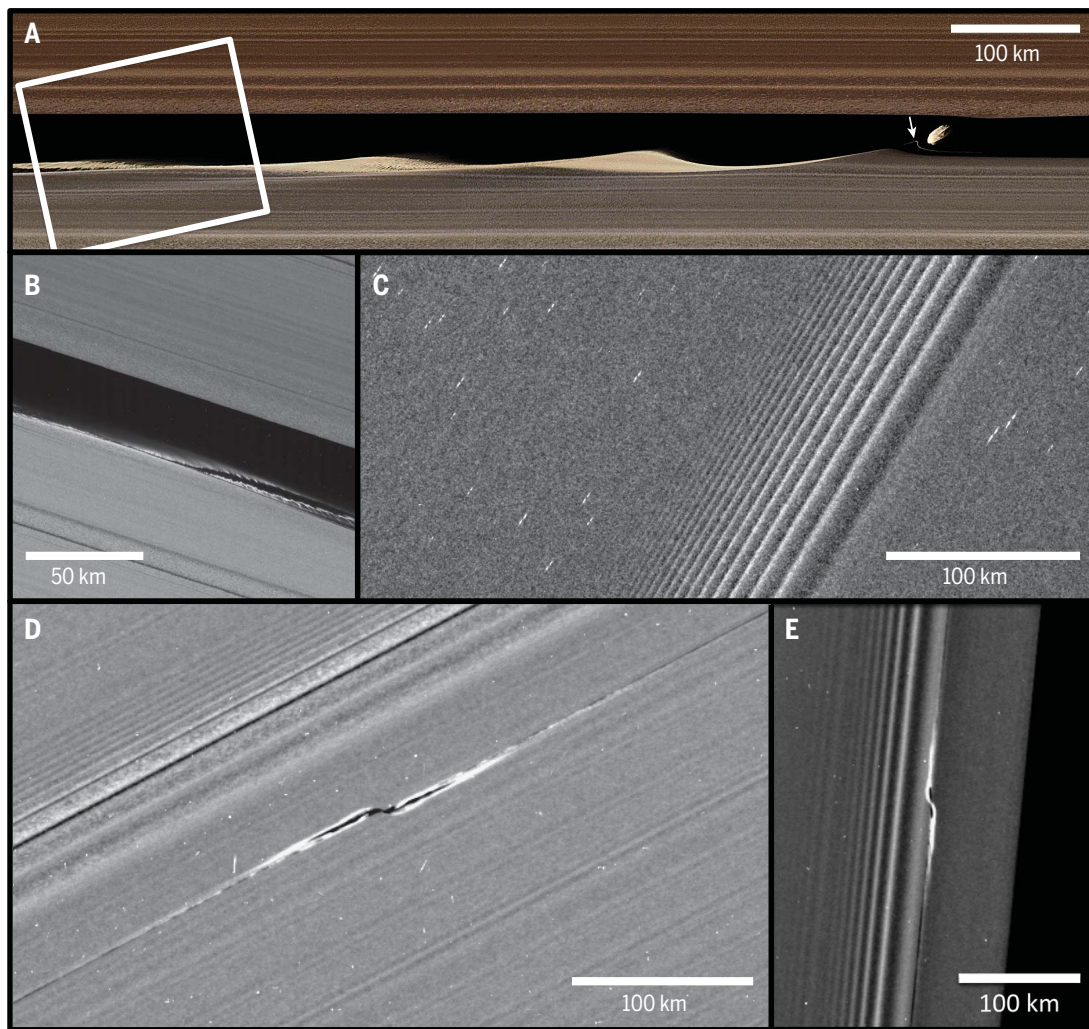
Fig. 1. Embedded moons cause structure in the main rings. (**A**) False-color image mosaic (4) showing Daphnis in the Keeler gap on the lit side of the rings, with three wave crests of the structure raised by Daphnis in the gap's outer edge. Each successive wave crest from right to left is older, having elapsed an additional orbital period (~13 hours) since its close approach to Daphnis. The direction to Saturn is up, and the orbital direction is to the right. A thin strand of material (indicated by the arrow) is present in the gap to the lower left of Daphnis, and there is intricate structure in the third wave crest downstream. The box on the left-hand side indicates the approximate footprint of the image in (B). (**B**) A further close-up of the third wave crest, on the unlit side of the rings. (**C**) Propellers in the Propeller Belts of the mid-A ring on the unlit side of the rings. The large multibanded structure across the center of the panel is the Prometheus 9:8 spiral density wave. (**D**) The propeller Blériot on the unlit side of the rings. (**E**) The propeller Earhart on the lit side of the rings.

magnified in Fig. 1B. Macroscopic clumps of ring particles, which are not visible in the first or second wave crest, dominate the third wave crest, as the effects of Daphnis diminish. Furthermore, a gap or rift appears between the clump-studded wave crest and the rest of the ring. We interpret this as a vertical feature: The ribbon of material may be rising above the ring plane, having been launched by the inclination of Daphnis, with the line of sight (due to Cassini's oblique viewing angle) passing through the vertical gap. As evidence for this, further downstream (in the left-hand portion of Fig. 1B), the same ribbon of material can be seen to pass behind the main portion of the ring, from Cassini's point of view. This hypothesis does not exclude some degree of simultaneous radial structure in the third wave crest. The difference in appearance between the third wave crest and the first two may be partly due to a shroud of smaller particles (whose structure perhaps is primarily radial) that smooths the appearance of the first two wave crests, which may have been absorbed into larger clumps in the third wave crest.

The propeller belts

The propellers observed (13) in close-range images taken during Saturn orbit insertion (SOI) were substantially smaller than those seen in the Propeller Belts during the remainder of the Cassini mission (14, 15). Figure 1C shows propellers of a size similar to those seen during SOI. We identified and analyzed 41 propellers in this image (4). We find a substantial range in propeller sizes, with the largest propellers being more than four times as large as the smallest (table S1). We also find that the population density, average size, and size distribution may vary substantially with ring radius on finer scales than previously identified (fig. S1), particularly in the vicinity of a moderately strong density wave. This implies that some combination of the parent bodies, subsequent evolution, and/or visibility of propellers is highly radially stratified.

Giant propellers

Close-range flyby images of propellers Blériot and Earhart are shown in Fig. 1, D and E, respectively. Blériot was captured on the unlit side of the rings, where regions can be dark because of low optical depth (insufficient material to scatter sunlight toward the camera) or because optical depths are so high that the region is opaque. Earhart was captured on the lit side, where brightness usually increases monotonically as a function of optical depth. Additionally, close-range flybys captured images of propeller Santos-Dumont on both the lit and unlit sides of the rings, in images taken on both sides of ring-plane crossing during a single RGO pass (fig. S2).

Complex structure is seen in all these images. The dark band through the center of Blériot, which is due to the disturbed region being opaque, extends further downstream than the similar dark band in the unlit-side image of Santos-Dumont, likely indicating higher surface mass densities.

Scalloping is present on the inner edges of the perturbed regions, analogous to patterns seen on the edges of the Encke and Keeler gaps. Equating the wavelength of the scalloping with $3\pi\Delta a$, and taking the full width of the gap (i.e., twice Δa) to be four times the Hill radius r_H (23), where $r_H \equiv a(m/3M)^{1/3}$ for Saturn's mass M and the central moon's mass m and semimajor axis a, we calculate $\Delta a \simeq 2r_H$ to be 1.0 km for Santos-Dumont and 1.6 km for Blériot.

The Hill radii imply masses of 7×10^{14} g for the central moon of Santos-Dumont and 3×10^{15} g for that of Blériot. Most likely, the actual size of each central moon is similar to its Hill radius (16), so that its bulk density is equal to the critical density for this region of the A ring, which is ~0.4 g cm^{-3} (24), so that the above-calculated Δa approximates the triaxial moon's longest axis.

The central propeller moon for each of these close-range propellers should be two to three pixels across in these images. However, we do not detect them, likely because they are obscured by the disturbed ring material swirling around them.

Ring structure: Texture belts

The main rings appear smooth in most images, although a clumpy straw-like texture has been identified in the troughs of strong density waves (25, 26). Other textures have been dimly perceptible in images throughout the Cassini mission but have not been described or analyzed in any detail.

The RGO and GF images show several classes of ring texture, in well-defined radial bands, which do not correlate with other ring properties. Examples of these textures are shown in Fig. 2.

There is growing evidence that some of the sharply bounded features in the main rings are not due to changes in surface mass density and thus must be due to variations in particle properties (27, 28). Composition, particle size, and regolith character (29) are candidate causes, although it is not clear how ring particles are sorted according to these properties. We find that these ring textures are localized to sharply defined radial bands (Fig. 2). We speculate that this may be due to differences in how ring particles bounce off each other when they collide and thus might be correlated with regolith character (30).

Clumpy straw-like texture is seen not only in the troughs of strong density waves (Fig. 2a) but also in smaller waves such as those due to Prometheus (Fig. 2B) and at other types of locations. At 124,230 km from Saturn's center (in the inner A ring), a region characterized by fine-scale radial structure that is not well understood, a 100-km radial band exhibits clumpy structure, whereas the regions around it do not (Fig. 2C). The clumpy texture at this location is correlated with a relatively bright band, but other relative brightness maxima nearby do not exhibit clumpy texture. The clumpy texture at this location is not associated with any spiral density wave, although such waves do occur at adjacent locations.

Many locations in the B ring (e.g., Fig. 2D) exhibit a more elongated texture. This streaky or feathery texture is often correlated with local minima in optical depths (although all optical depths are quite high in this region), which appear dark in lit-side images such as Fig. 2D. The landmark triple-humped belt in the outer Cassini Division also exhibits feathery texture (fig. S3). Here the dark (gap-like) streaks are more discrete and may be related to features termed "ghosts" identified in UVIS occultations (31).

Another streaky texture appears in all 10 of the narrow and sharp-edged increases in brightness and optical depth in the C ring known as "plateaux." For example, Plateau P1 (Fig. 2E) exhibits streaky texture, whereas the nonplateau C-ring material around it exhibits either clumpy texture or no texture at all. Plateau P5 also exhibits streaky texture (fig. S4). Their surface mass densities do not appear to be markedly different from those of the background C ring (32), so their defining characteristic must be related to particle properties (33).

An occultation of the star κ Orionis by the rings was observed using UVIS (4). Gaps ≥20 m across were seen in the plateaux, with an average separation of 0.5 to 1 km. We modeled the plateaux with a simplified bimodal transparency model using 19 UVIS stellar occultations (4). This model yields gap widths of 10 to 100 m and vertical thicknesses of the plateaux of 10 to 40 m. These average gap widths may represent the narrowest in a range of gap sizes, observable only with the high spatial resolution of the stellar occultations, with the dark streaks seen in the images being gaps on the wider end of the distribution.

Ring structure: F-ring objects

Images of the F-ring core obtained during the RGO and GF (Fig. 3) confirm the existence of a population of smaller objects by the detection of their associated mini-jets (34). Although the core has an irregular, jagged shape [figure 4 in (35)], the population of mini-jets visible in Fig. 3, D and E, are all in phase, implying that they formed from a set of objects that collided with the core almost simultaneously. This observation suggests that rather than representing a random population of small, colliding objects, the mini-jets in Fig. 3, D and E, had a common origin, probably as the result of a breakup of a single object. This supports previous inferences (36, 37) that impacts onto the rings may sometimes be due to Saturn-orbiting streams of material rather than to lone impacting objects. Additional evidence for this is shown in the inset to Fig. 3B, where a collection of objects extending over

Fig. 2. Belts of textures in the main rings. A strip along the bottom of each panel has been filtered by subtracting the average radial profile of the image, so that local structures and textures are more visible. All images in this figure show the lit side of the rings (4). (**A**) Straw-like clumps in the troughs of the strong Janus 6:5 density wave in the outer A ring. (**B**) Straw in the troughs of the Prometheus 26:25, 27:26, and 28:27 density waves (left to right) in the outer A ring. (**C**) Straw-like texture in one radial band of the inner A ring but not in surrounding regions. (**D**) Feathery texture in some radial bands of the outer B ring (especially those with lower brightness in the main part of the image) but not in surrounding regions. (**E**) Plateau P1 and its environs in the C ring, with three different textures in close proximity to each other.
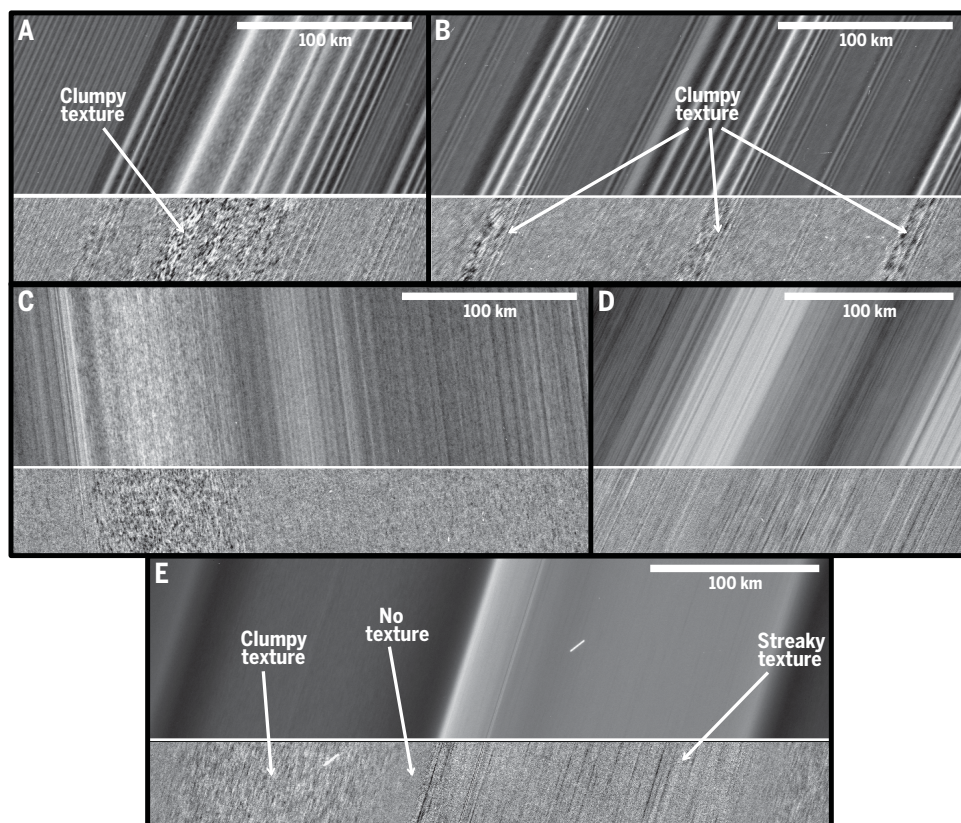
~0.05° (~100 km) appears to have recently emerged from the core. We interpret this feature as a more compact version of the multiple objects seen to cause the mini-jets in Fig. 3, D and E. The calculated radial velocities (4) of ~1.4 m s⁻¹ are consistent with those of previously observed mini-jets (34).

We observe a narrow component in the F ring, 1 to 2 km in radial extent but perhaps unresolved, located ~10 km radially inward of the center of the bright core and visible in ~50% of Fig. 3A (i.e., extending over ~2°). Although evidence for such a component has been seen before [figure 4h in (35)]), we infer from Fig. 3D that the original impact events that produced the mini-jet features in this part of the F ring originated when the source objects collided with the narrow component, implying the existence of substantial mass at this location. It has been suggested (38) that the true core of the F ring consists of discontinuous ring arcs, <1 km in radial width, each extending over ~2° in longitude, wherein most of the F ring's mass is contained. The observations in Fig. 3 do not constrain the mass of the F ring, but they do provide supporting evidence for this interpretation and imply that the true core of the F ring may be radially offset from the brighter components that are more commonly seen.

Ring composition, particle size, and grain size

The reflectance spectrum of Saturn's main rings in the ultraviolet (UV), visible, and near-infrared (IR) regions is dominated by fine-grained crystalline water ice with relatively small amounts of non-icy material (39, 40). The latter seems to consist of two distinct components. The first is responsible for the strong absorption at UV and blue wavelengths that gives the rings their pale tan or reddish color, and is now generally thought to be either organic in nature (41–43) or nanophase particles of metallic iron or iron oxides (44), whereas the second component is a spectrally neutral absorber generally assumed to be silicates and/or carbon (45). Together, this icy mixture makes up the regolith coating the surfaces of the individual ring particles, whose sizes range from a few millimeters up to ~5 m (39, 46–50).
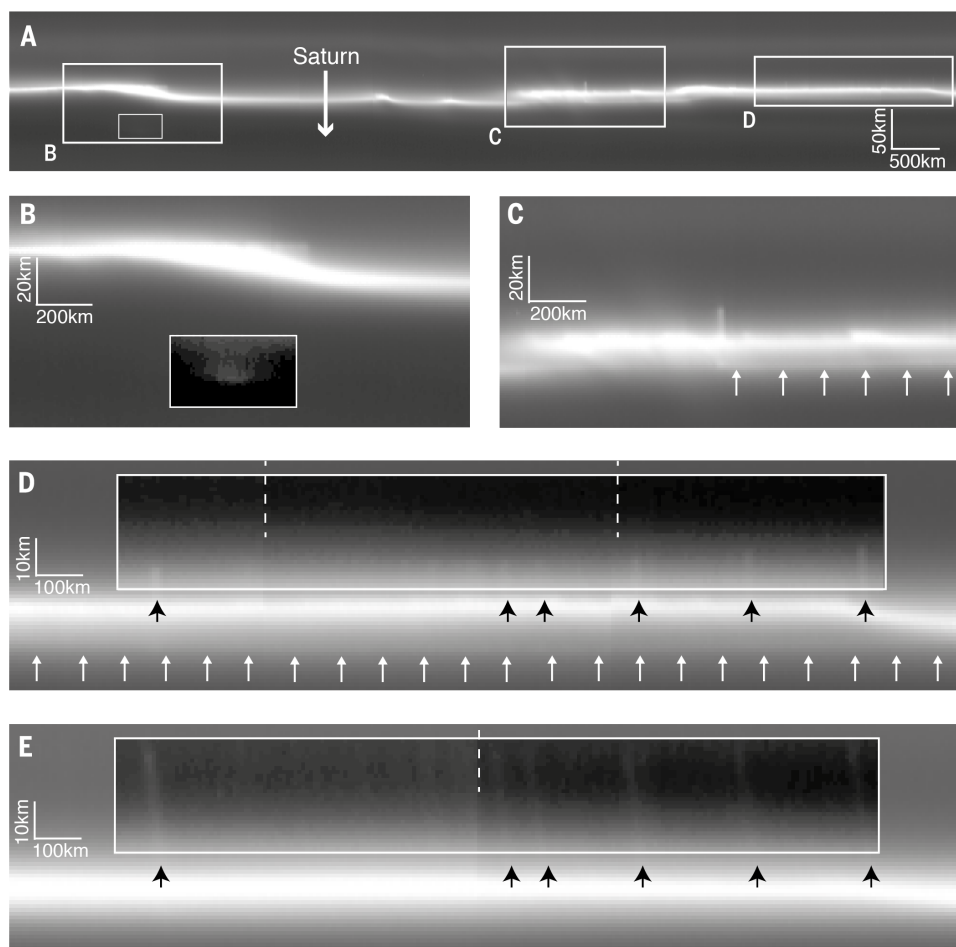
The UV absorber appears to be present as inclusions within the individual grains of water ice (sometimes referred to as an intramix), and its abundance increases monotonically with proximity to Saturn (51–53). Its nature has been debated (54), although it is suspected to be a primordial component of the rings. Recent observations and modeling (43) favor an organic material, perhaps tholins or mixtures of poly-

cyclic aromatic hydrocarbons (PAHs). Large organic molecules have been detected falling into Saturn's upper atmosphere (55), which may have come from the D ring. The neutral absorber, by contrast, is inferred to be intimately mixed with the icy grains (i.e., as separate particles in close proximity, like a mixture of salt and pepper) and is most abundant in the optically thin C ring and Cassini Division (52). It may be produced by the exposure of the originally pure icy rings to bombardment by interplanetary debris (45).

Previous observations by Cassini have shown small-scale spatial variations in the main rings' visible and near-IR spectrum (51, 56). VIMS spectra have revealed that regolith grains are larger in the A and B rings; grain size and/or composition varies locally in the vicinity of strong density waves in the A ring and at several locations in the B and C rings (52, 53, 57). UVIS optical depth variance measurements have yielded similar conclusions about small-scale variations in the ring particle-size distribution (33).

Color and spectral variations

During the final orbits of the Cassini mission, high-resolution multicolor and spectral scans were taken across the entire ring system, covering both the lit and unlit sides of the rings (Figs. 4 and 5).
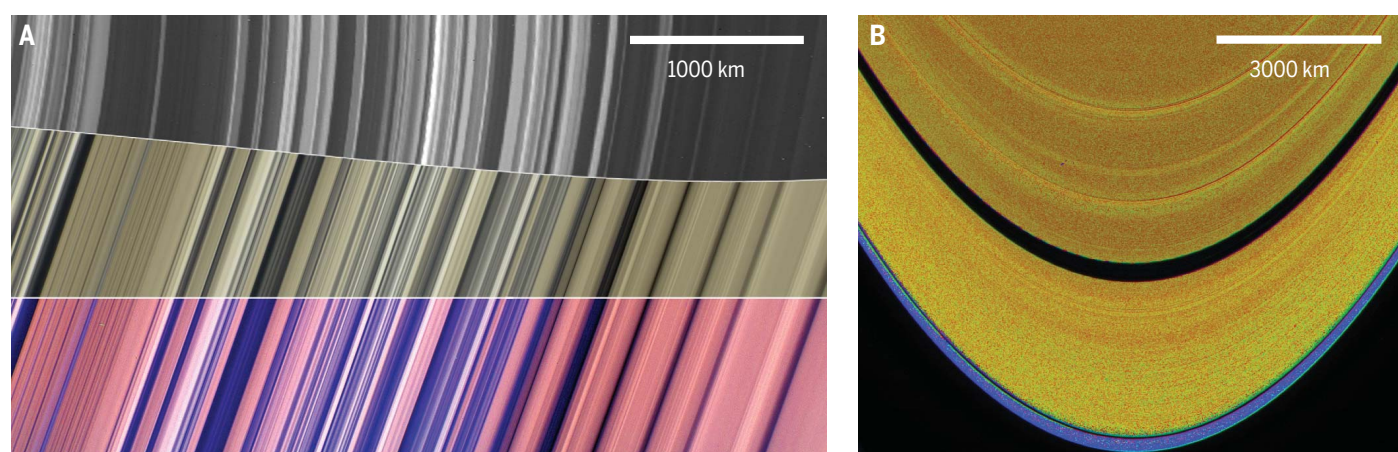
Fig. 3. Mini-jets and other structures in the F ring. A high-resolution mosaic (4) of the F-ring core region showing evidence for a population of small objects, their evolution, and a possible narrow component. (**A**) Context mosaic. White boxes indicate the regions shown in the other panels. (**B**) Enlarged portion of (A), showing a linear feature near the core with a contrast-enhanced inset showing a faint, linear feature below it. (**C**) Enlarged portion of (A), showing a mini-jet emerging ~10 km from the core with evidence of a narrow ring component parallel to and below the core. There is also evidence of a fan-shaped structure (4) to the left, characteristic of an embedded object on an eccentric orbit. (**D**) Enlarged portion of (A), with a region immediately above the core (indicated by the white rectangle) selectively contrast enhanced to bring out faint features. Several mini-jets (black arrows) emerge from the core, leaving trails that extend between ~7 km (left) and ~14 km (right) from the core. There is also evidence that the mini-jets originate in a narrow ring component parallel to the core but ~10 km below it (white arrows). (**E**) Same as (D), except portion of a different image mosaic of the same region, taken 85 min later. Although the resolution is poorer, the evolution of the mini-jets is evident, having doubled in length and undergone Keplerian shear. The dashed lines in (D) and (E) indicate longitudes where adjacent images overlap, leading to the production of slight offsets in the mosaics. The white arrows in (C) and (D) indicate the location of the narrow component.

Fig. 4. Color images of the B and A rings. (**A**) The inner-central B ring, covering the region from 98,600 to 105,500 km from Saturn's center at about 3 km px^{-1}. The top panel is a context image in black and white, while the middle and bottom panels are, respectively, true-color and enhanced-color versions. (**B**) The mid- and outer A ring (*4*). Figure S10 shows a VIMS image of the same region.

Color imaging with ISS was conducted at a resolution of ~3 km px^{-1}, although this is a lower resolution than for the black-and-white images (e.g., Figs. 1 and 2). Figure 4A displays a composite of true and enhanced color images (bottom two panels), with context given by a single unlit-face image (upper panel) in which darker bands are more optically thick. The pale tan color seen in the middle panel is generally not perceptible in a telescope, especially because Saturn is a yellowish tan itself (see below). Figure 4B is an enhanced color composite from early in the Cassini mission, illustrating the different color outward of the Keeler gap.

The observing mode for VIMS (*4*) resulted in a single, continuous image of the A, B, and C rings (referred to as a noodle) 64 pixels wide by ~1000 pixels long. The spatial resolution ranges from ~30 to 60 km px^{-1}, the gradient in resolution from one end of a noodle to the other being due to the changing spacecraft range. In the VIMS false-color images shown in Fig. 5, the red channel corresponds to the center of a strong water-ice absorption band, so reddish colors in the images signify less ice absorption, while the blue channel corresponds to a much weaker water-ice band. The green channel is a continuum wavelength. The red color is most evident in the C ring and Cassini Division but is also visible in the extreme outer part of the A ring. The inner B ring also has slightly weaker ice bands than do the outer B or A rings (*4*).

Figure 6 plots a set of standard spectral parameters for the main rings, derived from the VIMS lit-side scan on Rev 287 (*58*) and rebinned to a sampling interval of 20 km. Figure 6A shows two representative brightness profiles of the rings at continuum wavelengths. Figure 6C shows an optical depth profile of the rings for context, derived from a VIMS stellar occultation. In Fig. 6B are plotted water-ice band depths at 1.5 and 2.0 μm, calculated from the average spectrum for each radial bin (*4*). Also shown are spectral slopes in the visible portion of the spectrum, between 0.35 and 0.55 μm and between 0.55 and

0.85 μm (these are sometimes called the blue slope and the red slope, respectively, after the spectral regions where they are centered, rather than their shapes) Also plotted is the height of the 3.6-μm peak, which is defined by strong absorptions at 3 and ~4.5 μm, using the continuum level at 1.8 μm as a reference (*4*, *51*, *52*, *57*).

As seen in previous work (*51*, *52*), ice-band depths are greatest in the outer half of the B ring and the outer two-thirds of the A ring and lowest in the inner C ring and the Cassini Division. Band depths decrease smoothly from the middle A ring into the outer Cassini Division, and also from the innermost part of the B ring into the outer C ring, and then decrease further across the C ring. We confirm that regional transitions in band depths are gradual (*51*, *52*), except that we identify a more abrupt transition at the Keeler gap (see below). More detailed views of portions of Fig. 6 are shown in figs. S9 to S11.

Consistent with previous observations (*51*, *52*, *57*), we find that the fine-scale variations in the 0.35- to 0.55-μm slope and the IR water-ice band depths in the A and B rings are well correlated. These curves exhibit very similar shapes down to the spatial resolution limit of the scans, and these parameters are more closely correlated with each other than either is with the ring brightness I/F (*59*). The 0.35- to 0.55-μm slope and ice bands show different behaviors within the lower optical depth C ring and Cassini Division, as well as across the transitions between those rings and the innermost B and A rings. Detailed spectrophotometric modeling of VIMS observations of the A, B, and C rings (*40*, *52*) reveals that these varying trends can be attributed to a combination of variable particle regolith properties and compositions across the rings. For example, most of the fine-scale variations in the 0.35- to 0.55-μm slope and ice bands across the A and B rings can be attributed to shifts in grain sizes, whereas the deviations between these parameters in the lower optical depth C ring and Cassini Division are due to higher concentrations of darkening materials (neutral absorber) in those regions

(*40*). After accounting for these variations, the differences between the overall trends across the inner B ring between the 0.35- to 0.55-μm slope and the ice-band strengths could be due to an increase in the fractional abundances of the UV absorber closer to the planet (*52*).

Although the 0.55- to 0.85-μm slope shows some of the same features in the A and B rings as the other spectral parameters, its overall behavior is quite different and so traces a different aspect of the rings' texture or composition. In particular, the 0.55- to 0.85-μm slope is elevated in the middle part of the C ring, which is consistent with evidence for enhanced silicate or carbon-rich material at that location inferred from radio wavelengths (*60*).

A ring

In the A ring, halos of reduced water-ice band depth around the strong density waves are seen in the VIMS observations. In fig. S9, we plot the band depths in the A ring at a larger scale, together with profiles of the 0.35- to 0.55-μm and 0.55- 0.85-μm slopes (although the latter is fairly uniform in this region). Apart from the general inward decrease in band depths noted above, the most prominent features in the A ring profile are the peaks and dips seen at each of the strong density waves, especially those due to Janus. Centered on each of the Janus 4:3, 5:4, and 6:5 resonances is a peak in all ice-band depths—and in the 0.35- to 0.55-μm spectral slope—symmetrically flanked by a region of reduced band depths. These features have been dubbed "halos" (*51*), from VIMS SOI data. The overall radial width of each halo is ~1000 km, which is much larger than the extent of the density waves associated with these resonances, and the halos are centered on the waves. The halo associated with the Mimas 5:3 resonance is less evident, even though it is one of the strongest density waves in the A ring. (The nearby Mimas 5:3 bending wave at 131,800 km shows neither peak nor halo in the band depth profiles.) Although the reason for the peaks and halos remains unclear,

they may reflect an increase in the interparticle collision rate within the density wave itself (exposing fresh, coarser-grained ice from deeper layers in the ring particles), accompanied by the ejection of debris that falls back onto the surrounding regions (which may reduce their mean grain size by spreading a cloud of small icy particles). UVIS optical depth variance results support this conclusion (*33*).

There are several ripples in the band depths and 0.35- to 0.55-μm slope in the innermost part of the A ring, inwards of 124,500 km. There are two moderately strong density waves in this region, due to the Pandora 5:4 and Prometheus 6:5 resonances, and the optical depth profile shows several sharp peaks in this neighborhood, but there is no correlation between the band depths and either the resonances or optical depth structure (*61*).

The region around and outward of the Keeler gap is less red, shows less backscattering, and has weaker ice bands than the rest of the A ring, as noted first in Voyager data (*39, 62*), and pronounced color variations are seen in early Cassini images such as Fig. 4B, where the color transition is very sharp and coincides with the location of the gap. In our observations, the spectral variations appear to start near 136,200 km and extend across the gap to the ring's outer edge at 136,770 km. They include decreases in both ice-band depths and the 0.35- to 0.55-μm slope (figs. 6 and S9), accompanied by an increase in the continuum brightness of the rings beyond the Keeler gap. This region is also known to have a lower surface mass density (*63*) and different particle-size properties (*49, 50, 64*) from the rest of the A ring.

It remains unknown whether the spectral difference of the trans-Keeler region implies a different composition and origin of the underlying material, or whether some other factor is responsible. Figures 6B and S9 suggest weaker water-ice bands in the trans-Keeler region. This may imply less water ice and less of the accompanying organic reddening material. However, this hypothesis is difficult to reconcile with the relatively high reflectivity (I/F) in the same region, as seen in Fig. 6A and fig. S9. A finer regolith grain size outside the Keeler gap could explain all three observations: flatter (less-red) visual wavelength spectra, higher I/F, and weaker ice bands, whether or not the material has an intrinsically different composition.

B ring

The B ring, the most opaque and massive of Saturn's main rings (*65*), is conventionally divided into four or five subregions, based on varying structure and mean optical depth (*66*). The innermost or B1 region, between radii of 92,000 and 99,000 km, has a normal optical depth τ_n of 1 to 2 and is characterized by smooth, quasi-sinusoidal variations in τ_n and brightness with typical length scales of ~100 km (*67*). B1 is uniform in its spectral parameters (*51*) and in its optical colors (*68, 69*). Our VIMS data in Fig. 6 show very little variation in this region, except

for a modest inward increase in both the 0.35- to 0.55-μm and 0.55- to 0.85-μm slopes and a slight drop in the ice-band depths toward the C ring ramp over the innermost 500 km.

The B2 region is a zone of transition between the relatively low–optical depth B1 region and the opaque B3 region (outward of 104,000 km) where $\tau_n > 3$ almost everywhere and frequently exceeds 5. The B2 region is characterized by a series of abrupt local transitions in τ_n, between a minimum of ~2 and a maximum of 5 or greater, at irregular intervals of 40 to 200 km. The VIMS data for this region (shown at a larger scale in fig. S10) show a positive correlation between the IR ice-band depths, the 0.35- to 0.55-μm slope, and τ_n, with every peak (or dip) in band depth being associated with a maximum (or minimum) in τ_n. At somewhat lower spatial resolution, a similar relationship between optical depth and ice-band depths was previously demonstrated for the whole B ring (*52*); our data show that this correlation also holds down to the 50- to 100-km scale in the B2 region. The correlation of optical depth with I/F is much weaker, with peaks in τ_n being associated with both maxima and minima in I/F in this region. This suggests that many of the I/F variations in the central B ring are due to variations in albedo and/or phase function rather than particle density—a conclusion previously drawn from Voyager imaging data (*68*). Figure 4A shows a high-resolution ISS color image, also of the B2 region. There are sharp boundaries between the discrete ~100-km-wide bands in this region, which Cassini radio occultation data have shown to be even sharper than the ISS resolution (*66*). The narrow ringlets in the middle of this figure are about 40 km wide, whereas the broader bands near the right edge are 300 to 500 km across. It remains unclear what causes the variable brightness of these

ringlets and bands; the inherent reflectivity of the ring particle material, shadowing on their surfaces, their absolute abundance, and/or their packing density may all play a role. The bottom panel of Fig. 4A is a color-enhanced version of the middle panel, in which blue colors indicate a "less red" or flatter spectrum at visible wavelengths than the redder colors, which mean a steeper-than-average spectrum. Observations by Voyager showed these color variations at lower resolution (*68, 69*); we find that such well-defined color contrasts are sharply defined even down to the 3-km radial scale.

Across the very opaque B3 and B4 regions, between radii of 99,000 and 115,000 km (*66*), we find only small variations in the VIMS ice band depths or the 0.35- to 0.55-μm slope. A series of six low-amplitude oscillations in the band depths between 112,500 and 114,200 km are positively correlated with similar variations in both τ_n and I/F (*52*). Only within ~1300 km of the outer edge of the B ring is there a small but distinct decrease in all four of these spectral indicators, followed by an abrupt upturn in the final 500 km.

An exception to the generally flat band depths in this central part of the B ring is a broad but shallow dip in the ice band depths and 0.35- to 0.55-μm slope centered at 109,100 km and an even shallower dip centered at 107,400 km. These two features coincide with prominent peaks in I/F but with no obvious features in the optical depth profile. They may represent halos associated with the otherwise-invisible density waves that are expected to be driven by the Prometheus and Pandora 3:2 resonances (*52*), as seen in the A ring (fig. S9). Both dips are located 500 to 600 km exterior to the actual resonance locations (*52*). Two similar shallow dips in the band depths are seen in the outermost part of the B ring, at 115,700 and 116,500 km, and bear a
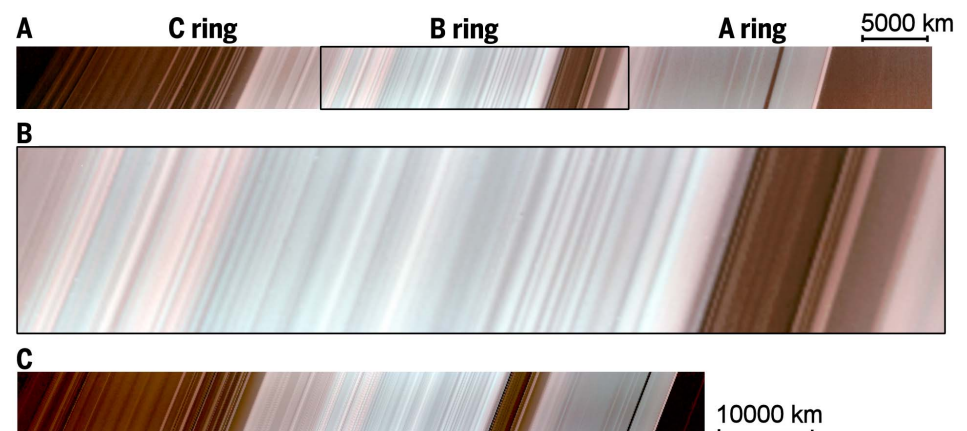

Fig. 5. Near-IR spectral scans. VIMS radial scans across the lit side of the main rings, displayed as false-color images. (**A**) The scan obtained on Rev 262, on 21 February 2017. (**B**) An enlarged view of the outer two-thirds of the B ring, and Cassini Division. (**C**) The scan obtained on Rev 287, on 7 August 2017. The scale bars indicate the average radial scale for each scan, although in both cases, the true scale varies across the scan because of the varying projected radial velocity of the spacecraft. On Rev 262, the velocity was a maximum in the B ring and the radial scale is compressed there by ~15%. On Rev 287, the velocity decreased from right to left by ~30% and the scale in the C ring is correspondingly stretched out.
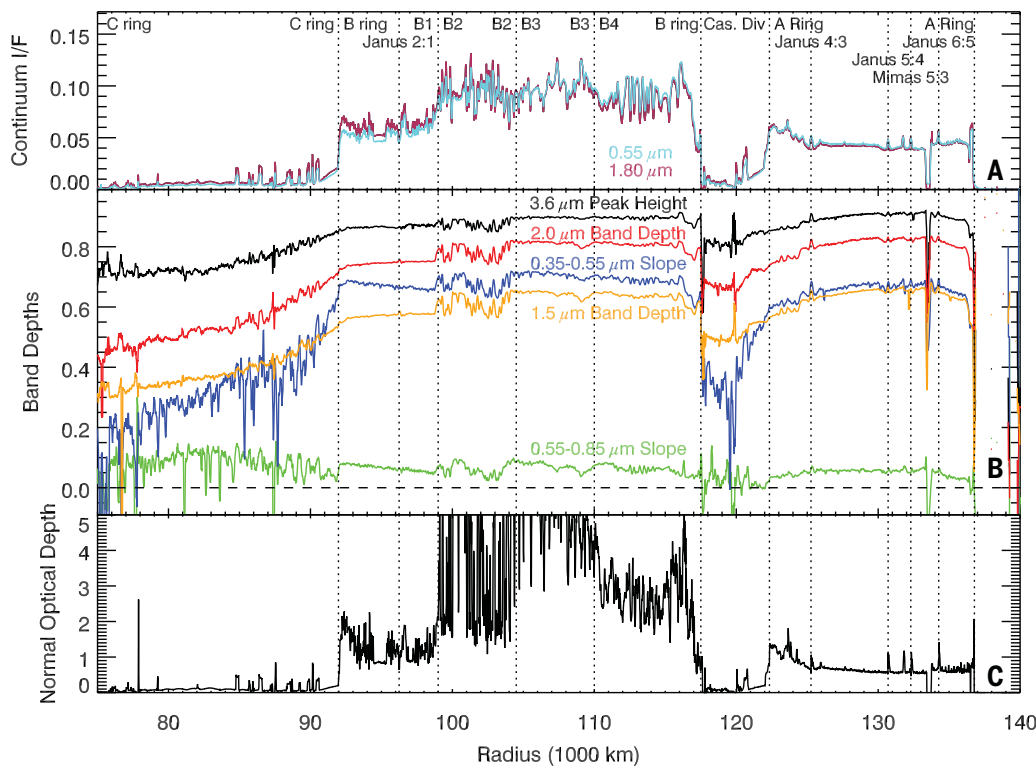
Fig. 6. Radial profiles of spectral parameters. Data shown are from the VIMS lit-side scan on Rev 287. Vertical dotted lines indicate (as labeled) the locations of density waves or of boundaries between ring regions, including the A, B, and C rings and the B-ring subregions B1 through B4. (**A**) Reflectivity of the rings at continuum wavelengths of 0.55 and 1.8 μm, with the locations of major ring boundaries and the strongest density waves identified by vertical dotted lines. (**B**) Fractional depths of the water-ice bands at 1.55, 2.0, and 3.6 μm in orange, red, and black, respectively, as well as the 0.35- to 0.55-μm and 0.55- to 0.85-μm slopes in blue and green (see text for definitions). (**C**) Optical depth profile of the rings obtained from a VIMS occultation of the star γ Crucis on Rev 082 (*52, 70*). Versions of this figure that zoom on the A, mid-B, and outer C rings, respectively, are shown in figs. S9, S10, and S11.

similar spatial relationship to the Enceladus 3:1 and Janus 3:2 resonances. This region is quite complex, with several other potentially interfering resonances due to Mimas and Prometheus (*70*).

C ring

Large-scale variations across the C ring visible in Fig. 6 include a steady inward decrease in IR-band depths and the 0.35- to 0.55-μm slope parameter. On a finer scale, the most obvious structural features in the C ring are the plateaus. A typical plateau is ~150 km wide, with fairly abrupt edges and a peak optical depth of ~0.4. They were detected in Voyager images (*1*) but are of unknown origin. Measurements of surface mass densities in the C ring (*32*) indicate that the plateau mass densities are similar to that of the adjacent background C ring ($\tau_n \simeq 0.1$), suggesting that their particle size distribution may be quite different (fewer particles in the meter-size range). VIMS observations at SOI yielded a marginal detection of variation in ice-band depths between the plateaus and background regions (*51*). There is no discernible signature of the plateaus in the lit-side profiles of ice band depths, but there is a weak enhancement in the 0.35- to 0.55-μm slope parameter, which may be due to a local increase in the abundance of the UV absorber (*52*).

In the outer C ring (fig. S11), the VIMS spectral data show that the 0.35- to 0.55-μm slope again tracks the depth of the ice band at 1.55 μm, although the profiles for the C ring are noisier at visible wavelengths. These data show very little difference, if any, in spectral characteristics between the plateaus and the background. In several cases, a very small increase in band depths

within the plateaus may be detectable, at the level of 0.01 or 0.02, or 1.5 to 3%. These signatures are more apparent in the 0.35- to 0.55-μm slope than in any of the IR ice bands.

Correlation with optical depth

Color variations and spectral variations often imply compositional variations. However, this is not necessarily correct in Saturn's rings. Figure 4A shows that ring color correlates with optical depth down to the smallest scales discernible: Optically thicker bands (darker in the top panel) are redder. A similar correlation between optical depth, ice-band depths, and spectral slope is visible in fig. S9 and discussed above. The intrinsic composition is unlikely to vary in such a correlated way and on such small radial scales. Meteoroid bombardment spreads ejecta around the rings on 100-km radial scales, smoothing out any such variations (*71*). However, variable optical depth might lead to other local changes in ring particle and/or ring layer properties. Collisional dynamics in regions of varying optical depth can lead to varying volume or packing density of particles, which might affect the degree of multiple interparticle scattering. Multiple scattering is known to enhance spectral contrast and the ring material is red, so more multiple scattering can make a region redder and also increase the relative depths of absorption bands (*72*). The local packing density can also lead to nonclassical scattering effects (e.g., shadowing), which can affect the ring brightness as a function of particle albedo, also affecting spectral contrast (*73*). The frequency and/or speed of collisions may also vary between regions of different optical depth, and this constant jostling can affect the roughness, porosity,

or grain size in the surfaces of the local particles (*30, 52, 74, 75*). Shadows on rough particle surfaces can change the particle phase function (*76*) in such a way as to exaggerate spectral contrasts at moderate to high phase angles. Monte Carlo models (*4*) of scattering in closely packed rings verified against similar models (*40, 73, 77*) suggest that the simplest explanation of the optical depth–dependent reddening is increased multiple scattering in the optically thicker regions by the already reddish ring particles, given particle phase functions and surface reflectances like those of the ring particles (*43*), in the geometry of the observation (the ISS image in Fig. 4A was taken at a relatively high phase angle, defined as Sun-target-observer angle, of α – 110°). At shorter wavelengths, particle albedos are low enough that multiple scattering is minimal, leading to the variable reddening. Therefore, the fine-scale color variations are consistent with a generally invariant composition, at least on 10- to 100-km length scales.

Ring temperature

CIRS measured the thermal emission from Saturn's main rings—the A, B, and C rings and the Cassini Division (*7, 78, 79*). During the RGOs, CIRS obtained radial scans at spatial resolutions ranging from 260 to 470 km for the A ring to 660 to 930 km for the C ring for both their lit (northern) and unlit (southern) sides. Temperature T of the ring material was derived from spectra measured with focal plane 1 (FP1) between 10 and 600 cm^{-1} (17 μm to 1 mm) at a spectral resolution of 15 cm^{-1}. Rings were viewed nearly face-on for both the lit and unlit sides at absolute spacecraft elevation angles B

(defined with respect to the ring plane) between 70° and 83°, and at phase angles of α ~ 60° for the lit side and α ~ 120° to 130° for the unlit side (table S2). The representative ring temperatures and associated scaling factors were derived from Planck functions fitted to FP1 spectral data (80).

The lit-side temperatures varied from 80 to 100 K, and the unlit-side temperatures varied from 70 to 90 K (Fig. 7). The radially averaged ring temperatures were [C, 93 K; B, 85 K; CD (Cassini Division), 88 K; A, 84 K] on the lit face and (C, 87 K; B, 73 K; CD, 80 K; A, 78 K) on the unlit face. Ring temperatures are driven by direct solar flux, solar flux reflected from Saturn, and Saturn thermal flux and depend on the transport of heat vertically through the rings via radiation, conduction, and particle transport. The flux due to Saturn-shine falls off approximately as the square of the distance from Saturn, and the solar flux varies with the sine of the solar elevation angle above the ring plane. The optically thin C ring and Cassini Division are warmer than the optically thick A and B rings because incident flux from the Sun and Saturn penetrates through the ring, resulting in more efficient heating (81). The magnitudes of the thermal radiation emitted from the lit and unlit sides of the C ring and Cassini Division are consistent with the unlit side being in thermal equilibrium with the radiation field. That is not true of the B and A rings, where the unlit sides radiate at a much higher temperature than would be expected if they were in equilibrium with the small amount of radiation that penetrates through the ring.

The heat transport within the C ring and Cassini Division is thought to be similar, although the C ring is always warmer than the Cassini Division because of its proximity to Saturn; similarly, the A- and B-ring temperatures are comparable, and at most epochs, the lit B ring is warmer than the lit A ring because of their relative distances from Saturn. This Saturn-shine effect is at a minimum for the current data because at solstice the solar flux is large compared to the Saturn-shine, so that the lit A-ring temperatures are comparable to those in the B ring. Details of the effect of Saturn-shine on the heating have been studied by using the radial dependence of temperature at Saturn Equinox when solar flux is nearly zero (81), where the effect of reduced mutual shadowing between particles in the optically thinner rings could be modeled directly, given details of the incident flux.

Within each ring, the temperature difference between the lit and unlit face correlates to some extent with optical depth, although the actual magnitudes of the temperatures differ between rings. The correlations are shown graphically in fig. S8 and discussed below with reference to Fig. 7. In the thick rings, this effect has been noted before and depends at least partially on efficiency of heat transport across the rings (82, 83). Detailed models indicate contributions to these broad trends from a positive correlation between albedo and optical depth across the rings (84), of a nature consistent with

preferential darkening of optically thinner rings due to meteoritic bombardment (45). Our observations show that, at finer scale, this correlation (of thermal gradient with optical depth) is not everywhere consistent, possibly because of local variations in ring structure and particle properties.

The temperature difference between the lit and unlit faces of the B ring correlates with optical depth, owing mostly to variation on the unlit face. This could be caused by mutual collisions between particles in high–optical depth regions hampering heat transport. Observational studies have shown that the thermal transmit-

tance of the B ring correlates inversely with optical depth (82). Transport models of the B ring based on effective medium theory indicate that if heat transport by the vertical motion of particles is negligible, then the observed correlation of the ring thermal gradient with optical depth can be explained only if the increase in optical depth is due to a vertically thicker ring and not to a larger filling factor (83).

Figure 7 indicates that in the A ring, the correlation of temperature differential with optical depth is consistent from the inner A ring to the flat outer regions, but there is a reverse in this trend in several locations where unlit-side
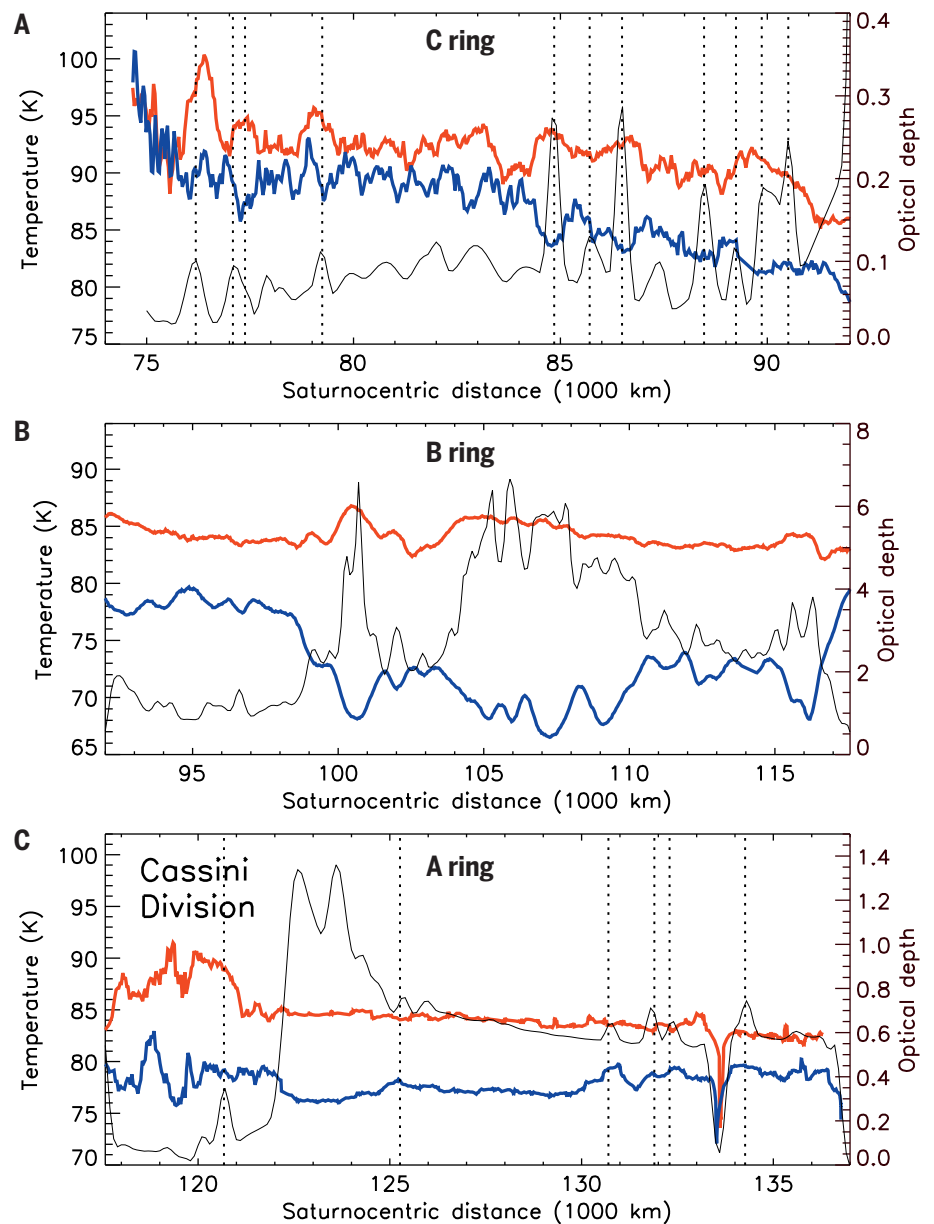

Fig. 7. Radial temperature profiles. Observations by CIRS of the lit (red) and unlit (blue) faces of (**A**) the C ring, (**B**) the B ring, and (**C**) the Cassini Division and the A ring. The black curve shows, for context, the optical depth measured by Cassini UVIS (8) and smoothed over a radial extent comparable to the typical CIRS footprint size. The vertical dotted lines show locations of prominent features: the plateaux in the C ring and the Cassini Division and the strongest density and bending waves in the A ring (table S3).

temperatures of the A ring have local maxima correlating with the halos of the strongest density waves (Janus 4:3, 5:4, and 6:5 and Mimas 5:3) and bending waves (Mimas 5:3). This decreases the temperature difference, even though the optical depths of these resonant locations are higher than those of the surrounding regions. This effect may be due to enhanced vertical heat transport or particle spin rates as a result of increased stirring of the ring particles in these regions. On the lit side of the rings, no temperature differences between the resonant locations and their surrounding regions are seen.

Correlations between temperature gradient and optical depth are not obvious in the C ring and Cassini Division, partially because of the lower signal-to-noise ratio in those regions. There appear to be dips in the unlit-side temperature within at least the largest plateaus. In contrast to the B and A rings, where the lit-side temperature varies little, there are features in the lit-side temperature of the C ring, but these do not correlate well with the optical depth. The net result is that there is either a weak correlation or none between optical depth and temperature difference in the optically thin regions and that other effects seem to be important in this regard. Temperature maxima near the largest plateaus could be associated with mutual heating between particles (84) or could be associated with radial variations in particle properties or ring structure, the presence of which is hinted at by the streaky texture seen in images of the C-ring plateaus.

Measurements by VIMS of the wavelength of the broad continuum peak around ~3.6 m can be used to infer the surface temperature of water ice. This method is applicable to ring particles, for which water ice is the dominant endmember (53). Spatial and temporal variations of the temperature as derived by this method are seen in the RGO and GF lit-side data. For most of the A ring, this peak was found at about 3.58 μm, corresponding to $T \sim 88$ K, with lower temperatures in the outermost parts of the ring. The same temperature prevails inward to the mid-B ring, but it increases to $T \sim 107$ K (peak at 3.60 μm) in the inner B ring. In the C ring and Cassini Division, the 3.6-μm reflectance peak is faint and distorted by Saturn-shine, making temperature retrieval uncertain. However, data collected before the GF (53) have shown systematically higher temperatures; the inner C ring is 30 K warmer than the B ring, and the Cassini Division is 20 K warmer than the outer A ring. These VIMS results mirror the large-scale variations in mean albedo and optical depth, in the sense that the particles are colder where these quantities are higher. Furthermore, with the exception of the Cassini Division, the ring temperature decreases with distance from Saturn (53). However, the temperatures inferred by VIMS are generally higher than those measured by CIRS. Different depths to which ring particles are penetrated by the radiation measured by VIMS (~1 mm) and CIRS ($\gtrsim 10$ mm) may play a role, as may the larger-pixel footprint for CIRS, which could average warmer and cooler temperatures together.

Conclusions

We have reported imaging and spectral observations of Saturn's rings taken during the final year of the Cassini mission. The rings are sculpted by embedded masses, producing structure visible down to our resolution limit. Correlations of spectral properties and temperature with optical depth are tight at many locations, although exceptions are found in certain regions already known to be enigmatic. Some spectral variations may be due to local variations in optical depth, rather than being solely due to particle composition or regolith grain size. Sharply stratified variations in particle properties, possibly including regolith character and bulk porosity as well as the distribution of particle sizes, likely play a role in producing many of the structures described here, and in some cases they may supplant variations in surface mass density as the dominant effect.

REFERENCES AND NOTES

1. J. N. Cuzzi, G. Filacchione, E. A. Marouf, *Planetary Ring Systems: Properties, Structure, and Evolution*, M. S. Tiscareno, C. D. Murray, Eds. (Cambridge Univ. Press, 2018), pp. 51–92.
2. Optical depth τ quantifies the attenuation of a beam of light passing through the disk, measured in e-folding terms. That is, $\tau \equiv -\ln\mathcal{T}$ for the fractional transparency $\mathcal{T}$. The normal optical depth τ_n corrects for the effects of an inclined line of sight, thus approximating what the optical depth would be if the line of sight were normal to the ring plane (that is, if observed face-on to the rings).
3. M. M. Hedman, F. Postberg, D. P. Hamilton, S. Renner, H.-W. Hsu, *Planetary Ring Systems: Properties, Structure, and Evolution*, M. S. Tiscareno, C. D. Murray, Eds. (Cambridge Univ. Press, 2018), pp. 308–337.
4. Materials and methods are available as supplementary materials.
5. C. C. Porco et al., Cassini imaging science: Instrument characteristics and anticipated scientific investigations at Saturn. *Space Sci. Rev.* **115**, 363–497 (2004). doi: 10.1007/s11214-004-1456-7
6. R. H. Brown et al., The Cassini Visual and Infrared Mapping Spectrometer (Vims) Investigation. *Space Sci. Rev.* **115**, 111–168 (2004). doi: 10.1007/s11214-004-1453-x
7. F. M. Flasar et al., Exploring The Saturn System In The Thermal Infrared: The Composite Infrared Spectrometer. *Space Sci. Rev.* **115**, 169–297 (2004). doi: 10.1007/s11214-004-1454-9
8. J. E. Colwell et al., Cassini UVIS stellar occultation observations of Saturn's rings. *Astron. J.* **140**, 1569–1578 (2010). doi: 10.1088/0004-6256/140/6/1569
9. P. Goldreich, S. Tremaine, The Dynamics of Planetary Rings. *Annu. Rev. Astron. Astrophys.* **20**, 249–283 (1982). doi: 10.1146/annurev.aa.20.090182.001341
10. F. H. Shu, *Planetary Rings*, R. Greenberg, A. Brahic, Eds. (Univ. of Arizona Press, Tucson, 1984), pp. 513–561.
11. M. S. Tiscareno, J. A. Burns, P. D. Nicholson, M. M. Hedman, C. C. Porco, Cassini imaging of Saturn's rings. *Icarus* **189**, 14–34 (2007). doi: 10.1016/j.icarus.2006.12.025
12. F. Spahn et al., *Planetary Ring Systems: Properties, Structure, and Evolution*, M. S. Tiscareno, C. D. Murray, Eds. (Cambridge Univ. Press, 2018), pp. 157–197.
13. M. S. Tiscareno et al., 100-metre-diameter moonlets in Saturn's A ring from observations of 'propeller' structures. *Nature* **440**, 648–650 (2006). doi: 10.1038/nature04581; pmid: 16572165
14. M. Sremčević et al., A belt of moonlets in Saturn's A ring. *Nature* **449**, 1019–1021 (2007). doi: 10.1038/nature06224; pmid: 17960236
15. M. S. Tiscareno, J. A. Burns, M. M. Hedman, C. C. Porco, The population of propellers in Saturn's A ring. *Astron. J.* **135**, 1083–1091 (2008). doi: 10.1088/0004-6256/135/3/1083
16. M. S. Tiscareno et al., Physical characteristics and non-Keplerian orbital motion of "propeller" moons embedded in Saturn's rings. *Astrophys. J.* **718**, L92–L96 (2010). doi: 10.1088/2041-8205/718/2/L92
17. B. J. Buratti et al., Close Cassini flybys of Saturn's ring moons Pan, Daphnis, Atlas, Pandora, and Epimetheus. *Science* **364**, eaat2349 (2019).
18. Keplerian shear is the difference in orbital velocity between adjacent streamlines of ring material. For angular velocity n and radial distance a from Saturn's center, it is straightforward to differentiate Kepler's third law and obtain $dn/da = (3/2)(n/a)$.
19. J. W. Weiss, C. C. Porco, M. S. Tiscareno, Ring edge waves and the masses of nearby satellites. *Astron. J.* **138**, 272–286 (2009). doi: 10.1088/0004-6256/138/1/272
20. M. S. Tiscareno et al., AAS Division for Planetary Sciences Meeting Abstracts **37**, 64.02 (2005).
21. P. A. Torrey, M. S. Tiscareno, J. A. Burns, C. C. Porco, AAS Division on Dynamical Astronomy Meeting Abstracts **39**, 15.19 (2008).
22. R. Tajeddine et al., Dynamical phenomena at the inner edge of the Keeler gap. *Icarus* **289**, 80–93 (2017). doi: 10.1016/j.icarus.2017.02.002
23. M. Seiß, F. Spahn, M. Sremčević, H. Salo, Structures induced by small moonlets in Saturn's rings: Implications for the Cassini Mission. *Geophys. Res. Lett.* **32**, L11205 (2005). doi: 10.1029/2005GL022506
24. M. S. Tiscareno, M. M. Hedman, J. A. Burns, J. C. Castillo-Rogez, Compositions and origins of outer planet systems: insights from the Roche critical density. *Astrophys. J.* **765**, L28 (2013). doi: 10.1088/2041-8205/765/2/L28
25. C. C. Porco et al., Cassini Imaging Science: Initial results on Saturn's rings and small satellites. *Science* **307**, 1226–1236 (2005). doi: 10.1126/science.1108056; pmid: 15731439
26. M. C. Lewis, G. R. Stewart, Expectations for Cassini observations of ring material with nearby moons. *Icarus* **178**, 124–143 (2005). doi: 10.1016/j.icarus.2005.04.009
27. M. S. Tiscareno, M. M. Hedman, J. A. Burns, J. W. Weiss, C. C. Porco, Probing the inner boundaries of Saturn's A ring with the Iapetus −1:0 nodal bending wave. *Icarus* **224**, 201–208 (2013). doi: 10.1016/j.icarus.2013.02.026
28. M. M. Hedman, P. D. Nicholson, Kronoseismology: using density waves in Saturn's C ring to probe the planet's interior. *Astron. J.* **146**, 12 (2013). doi: 10.1088/0004-6256/146/1/12
29. Regolith is any layer of loose surface material.
30. E. Déau et al., The opposition effect in Saturn's main rings as seen by Cassini ISS: 4. Correlations of the surge morphology with surface albedos and VIMS spectral properties. *Icarus* **305**, 324–349 (2018). doi: 10.1016/j.icarus.2017.12.025
31. K. Baillié, J. E. Colwell, L. W. Esposito, M. C. Lewis, Meter-sized moonlet population in Saturn's C ring and Cassini Dy. *Astron. J.* **145**, 171 (2013). doi: 10.1088/0004-6256/145/6/171
32. M. M. Hedman, P. D. Nicholson, More Kronoseismology with Saturn's rings. *Mon. Not. R. Astron. Soc.* **444**, 1369–1388 (2014). doi: 10.1093/mnras/stu1503
33. J. E. Colwell, L. W. Esposito, J. H. Cooney, Particle sizes in Saturn's rings from UVIS stellar occultations 1. Variations with ring region. *Icarus* **300**, 150–166 (2018). doi: 10.1016/j.icarus.2017.08.036
34. N. O. Attree, C. D. Murray, G. A. Williams, N. J. Cooper, A survey of low-velocity collisional features in Saturn's F ring. *Icarus* **227**, 56–66 (2014). doi: 10.1016/j.icarus.2013.09.008
35. C. D. Murray et al., The determination of the structure of Saturn's F ring by nearby moonlets. *Nature* **453**, 739–744 (2008). doi: 10.1038/nature06999; pmid: 18528389
36. M. S. Tiscareno et al., Observations of ejecta clouds produced by impacts onto Saturn's rings. *Science* **340**, 460–464 (2013). doi: 10.1126/science.1233524; pmid: 23620048
37. M. M. Hedman, J. A. Burns, M. R. Showalter, Corrugations and eccentric spirals in Saturn's D ring: New insights into what happened at Saturn in 1983. *Icarus* **248**, 137–161 (2015). doi: 10.1016/j.icarus.2014.10.021
38. J. N. Cuzzi et al., Saturn's F Ring core: Calm in the midst of chaos. *Icarus* **232**, 157–175 (2014). doi: 10.1016/j.icarus.2013.12.027
39. J. Cuzzi et al., *Saturn from Cassini-Huygens*, M. Dougherty, L. Esposito, S. M. Krimigis, Eds. (Springer, 2009), pp. 459–509.
40. M. Ciarniello et al., Cassini-VIMS observations of Saturn's main rings: II. A spectrophotometric study by means of Monte Carlo ray-tracing and Hapke's theory. *Icarus* **317**, 242–265 (2019). doi: 10.1016/j.icarus.2018.07.010
41. F. Poulet, J. N. Cuzzi, The Composition of Saturn's Rings. *Icarus* **160**, 350–358 (2002). doi: 10.1006/icar.2002.6967
42. F. Poulet, D. P. Cruikshank, J. N. Cuzzi, T. L. Roush, R. G. French, Compositions of Saturn's rings A, B, and C from high resolution near-infrared spectroscopic observations. *Astron. Astrophys.* **412**, 305–316 (2003). doi: 10.1051/0004-6361:20031123

43. J. N. Cuzzi *et al*., HST-STIS spectra and the redness of Saturn's rings. *Icarus* **309**, 363–388 (2018). doi: 10.1016/j.icarus.2018.02.025

44. R. N. Clark *et al*., The surface composition of Iapetus: Mapping results from Cassini VIMS. *Icarus* **218**, 831–860 (2012). doi: 10.1016/j.icarus.2012.01.008

45. J. N. Cuzzi, P. R. Estrada, Compositional Evolution of Saturn's Rings Due to Meteoroid Bombardment. *Icarus* **132**, 1–35 (1998). doi: 10.1006/icar.1997.5863

46. E. A. Marouf, G. L. Tyler, H. A. Zebker, R. A. Simpson, V. R. Eshleman, Particle size distributions in Saturn's rings from voyager 1 radio occultation. *Icarus* **54**, 189–211 (1983). doi: 10.1016/0019-1035(83)90192-6

47. H. A. Zebker, E. A. Marouf, G. L. Tyler, Saturn's rings: Particle size distributions for thin layer models. *Icarus* **64**, 531–548 (1985). doi: 10.1016/0019-1035(85)90074-0

48. R. G. French, P. D. Nicholson, Saturn's Rings II Particle Sizes Inferred from Stellar Occultation Data. *Icarus* **145**, 502–523 (2000). doi: 10.1006/icar.2000.6357

49. R. A. Harbison, P. D. Nicholson, M. M. Hedman, The smallest particles in Saturn's A and C Rings. *Icarus* **226**, 1225–1240 (2013). doi: 10.1016/j.icarus.2013.08.015

50. T. M. Becker, J. E. Colwell, L. W. Esposito, A. D. Bratcher, Characterizing the particle size distribution of Saturn's A ring with Cassini UVIS occultation data. *Icarus* **279**, 20–35 (2016). doi: 10.1016/j.icarus.2015.11.001

51. P. D. Nicholson *et al*., A close look at Saturn's rings with Cassini VIMS. *Icarus* **193**, 182–212 (2008). doi: 10.1016/j.icarus.2007.08.036

52. M. M. Hedman *et al*., Connections between spectra and structure in Saturn's main rings based on Cassini VIMS data. *Icarus* **223**, 105–130 (2013). doi: 10.1016/j.icarus.2012.10.014

53. G. Filacchione *et al*., Cassini–VIMS observations of Saturn's main rings: I. Spectral properties and temperature radial profiles variability with phase angle and elevation. *Icarus* **241**, 45–65 (2014). doi: 10.1016/j.icarus.2014.06.001

54. J. N. Cuzzi *et al*., An evolving view of Saturn's dynamic rings. *Science* **327**, 1470–1475 (2010). doi: 10.1126/science.1179118; pmid: 20299586

55. J. H. Waite Jr. *et al*., Chemical interactions between Saturn's atmosphere and its rings. *Science* **362**, eaat2382 (2018). doi: 10.1126/science.aat2382; pmid: 30287634

56. R. H. Brown *et al*., Observations in the Saturn system during approach and orbital insertion, with Cassini's visual and infrared mapping spectrometer (VIMS). *Astron. Astrophys.* **446**, 707–716 (2006). doi: 10.1051/0004-6361:20053054

57. G. Filacchione *et al*., Saturn's icy satellites and rings investigated by Cassini–VIMS: III – Radial compositional variability. *Icarus* **220**, 1064–1096 (2012). doi: 10.1016/j.icarus.2012.06.040

58. The Rev code is a three-digit label for Cassini's orbits around Saturn. For operational reasons, Saturn orbit insertion (SOI) was followed by Revs 00A, 00B, and 00C, and then by Revs 003 through 293.

59. *I/F* is a measure of the observed brightness *I* as normalized by a perfect Lambert surface's reflection of the incident solar flux π*F*.

60. Z. Zhang *et al*., Cassini microwave observations provide clues to the origin of Saturn's C ring. *Icarus* **281**, 297–321 (2017). doi: 10.1016/j.icarus.2016.07.020

61. The sharp peak at 123,570 km in both τ$_n$ and *I/F* is probably associated with the Prometheus resonance.

62. L. Dones, J. N. Cuzzi, M. R. Showalter, Voyager Photometry of Saturn's A Ring. *Icarus* **105**, 184–215 (1993). doi: 10.1006/icar.1993.1118

63. M. S. Tiscareno, B. E. Harris, Mapping spiral waves and other radial features in Saturn's rings. *Icarus* **312**, 157–171 (2018). doi: 10.1016/j.icarus.2018.04.023

64. R. G. Jerousek, J. E. Colwell, L. W. Esposito, P. D. Nicholson, M. M. Hedman, Small particles and self-gravity wakes in Saturn's rings from UVIS and VIMS stellar occultations. *Icarus* **279**, 36–50 (2016). doi: 10.1016/j.icarus.2016.04.039

65. L. Iess *et al*., Measurement and implications of Saturn's gravity field and ring mass. *Science* **364**, eaat2965 (2019).

66. J. E. Colwell *et al*., *Saturn from Cassini-Huygens*, M. Dougherty, L. Esposito, S. M. Krimigis, Eds. (Springer, 2009), pp. 375–412.

67. L. J. Horn, J. N. Cuzzi, Characteristic Wavelengths of Irregular Structure in Saturn's B Ring. *Icarus* **119**, 285–310 (1996). doi: 10.1006/icar.1996.0021

68. P. R. Estrada, J. N. Cuzzi, Voyager Observations of the Color of Saturn's Rings. *Icarus* **122**, 251–272 (1996). doi: 10.1006/icar.1996.0124

69. P. R. Estrada, J. N. Cuzzi, M. R. Showalter, Voyager color photometry of Saturn's main rings: A correction. *Icarus* **166**, 212–222 (2003). doi: 10.1016/j.icarus.2003.06.001

70. M. M. Hedman, P. D. Nicholson, The B-ring's surface mass density from hidden density waves: Less than meets the eye? *Icarus* **279**, 109–124 (2016). doi: 10.1016/j.icarus.2016.01.007

71. P. R. Estrada, R. H. Durisen, J. N. Cuzzi, D. A. Morgan, Combined structural and compositional evolution of planetary rings due to micrometeoroid impacts and ballistic transport. *Icarus* **252**, 415–439 (2015). doi: 10.1016/j.icarus.2015.02.005

72. F. Poulet, J. N. Cuzzi, D. P. Cruikshank, T. Roush, C. M. Dalle Ore, Comparison between the Shkuratov and Hapke Scattering Theories for Solid Planetary Surfaces: Application to the Surface Composition of Two Centaurs. *Icarus* **160**, 313–324 (2002). doi: 10.1006/icar.2002.6970

73. H. Salo, R. G. French, The opposition and tilt effects of Saturn's rings from HST observations. *Icarus* **210**, 785–816 (2010). doi: 10.1016/j.icarus.2010.07.002

74. E. Déau *et al*., The opposition effect in Saturn's main rings as seen by Cassini ISS: 1. Morphology of phase functions and dependence on the local optical depth. *Icarus* **226**, 591–603 (2013). doi: 10.1016/j.icarus.2013.01.015

75. E. Déau, The opposition effect in Saturn's main rings as seen by Cassini ISS: 2. Constraints on the ring particles and their regolith with analytical radiative transfer models. *Icarus* **253**, 311–345 (2015). doi: 10.1016/j.icarus.2013.08.031

76. J. N. Cuzzi, L. B. Chambers, A. R. Hendrix, Rough surfaces: Is the dark stuff just shadow? *Icarus* **289**, 281–294 (2017). doi: 10.1016/j.icarus.2016.10.018

77. C. C. Porco *et al*., Simulations of the dynamical and light-scattering behavior of Saturn's rings and the derivation of ring particle and disk properties. *Astron. J.* **136**, 2172–2200 (2008). doi: 10.1088/0004-6256/136/5/2172

78. V. G. Kunde *et al*., in *Proc. SPIE Vol. 2803, Cassini/Huygens: A Mission to the Saturnian Systems*, L. Horn, Ed. (SPIE, 1996), pp. 162–177.

79. D. E. Jennings *et al*., Composite infrared spectrometer (CIRS) on Cassini. *Appl. Opt.* **56**, 5274–5294 (2017). doi: 10.1364/AO.56.005274; pmid: 29047582

80. L. J. Spilker *et al*., Cassini thermal observations of Saturn's main rings: Implications for particle rotation and vertical mixing. *Planet. Space Sci.* **54**, 1167–1176 (2006). doi: 10.1016/j.pss.2006.05.033

81. L. Spilker, C. Ferrari, R. Morishima, Saturn's ring temperatures at equinox. *Icarus* **226**, 316–322 (2013). doi: 10.1016/j.icarus.2013.06.002

82. S. Pilorz, N. Altobelli, J. Colwell, M. Showalter, Thermal transport in Saturn's B ring inferred from Cassini CIRS. *Icarus* **254**, 157–177 (2015). doi: 10.1016/j.icarus.2015.01.002

83. E. Reffet, M. Verdier, C. Ferrari, Thickness of Saturn's B ring as derived from seasonal temperature variations measured by Cassini CIRS. *Icarus* **254**, 276–286 (2015). doi: 10.1016/j.icarus.2015.04.006

84. R. Morishima *et al*., A multilayer model for thermal infrared emission of Saturn's rings II: Albedo, spins, and vertical mixing of ring particles inferred from Cassini CIRS. *Icarus* **210**, 330–345 (2010). doi: 10.1016/j.icarus.2010.06.032

ACKNOWLEDGMENTS

SUPPLEMENTARY MATERIALS

Science

Close-range remote sensing of Saturn's rings during Cassini's ring-grazing orbits and Grand Finale

Matthew S. Tiscareno, Philip D. Nicholson, Jeffrey N. Cuzzi, Linda J. Spilker, Carl D. Murray, Matthew M. Hedman, Joshua E. Colwell, Joseph A. Burns, Shawn M. Brooks, Roger N. Clark, Nicholas J. Cooper, Estelle Deau, Cecile Ferrari, Gianrico Filacchione, Richard G. Jerousek, Stéphane Le Mouélic, Ryuji Morishima, Stu Pilorz, Sébastien Rodriguez, Mark R. Showalter, Sarah V. Badman, Emily J. Baker, Bonnie J. Buratti, Kevin H. Baines and Christophe Sotin

Cassini's last look at Saturn's rings

During the final stages of the Cassini mission, the spacecraft flew between the planet and its rings, providing a new view on this spectacular system (see the Perspective by Ida). Setting the scene, Spilker reviews the numerous discoveries made using Cassini during the 13 years it spent orbiting Saturn. Iess *et al.* measured the gravitational pull on Cassini, separating the contributions from the planet and the rings. This allowed them to determine the interior structure of Saturn and the mass of its rings. Buratti *et al.* present observations of five small moons located in and around the rings. The moons each have distinctive shapes and compositions, owing to accretion of ring material. Tiscareno *et al.* observed the rings directly at close range, finding complex features sculpted by the gravitational interactions between moons and ring particles. Together, these results show that Saturn's rings are substantially younger than the planet itself and constrain models of their origin.

Science, this issue p. 1046, p. eaat2965, p. eaat2349, p. eaau1017; see also p. 1028

ARTICLE TOOLS	http://science.sciencemag.org/content/364/6445/eaau1017
SUPPLEMENTARY MATERIALS	http://science.sciencemag.org/content/suppl/2019/06/12/364.6445.eaau1017.DC1
RELATED CONTENT	http://science.sciencemag.org/content/sci/364/6445/1028.full http://science.sciencemag.org/content/sci/364/6445/eaat2965.full http://science.sciencemag.org/content/sci/364/6445/eaat2349.full
REFERENCES	This article cites 93 articles, 7 of which you can access for free http://science.sciencemag.org/content/364/6445/eaau1017#BIBL
PERMISSIONS	http://www.sciencemag.org/help/reprints-and-permissions

Use of this article is subject to the Terms of Service